PREDICTING CHAR YIELD OF HIGH-TEMPERATURE RESINS

Jacob R. Gissinger[1], Scott R. Zavada[1], Joseph G. Smith[1], Josh Kemppainen[2], Ivan Gallegos[2], Gregory Odegard[2], Emilie J. Siochi[1] and Kristopher E. Wise[1]

[1]Advanced Materials and Processing Branch, NASA Langley Research Center, Hampton, Virginia 23681, United States

[2]Department of Mechanical Engineering and Engineering Mechanics, Michigan Technological University, Houghton, MI, 49931, United States

ABSTRACT

A simulation technique has been developed for predicting the char yield of organic resins during high-temperature processing. In silico methods can aid in the screening of new advanced materials for a number of important properties, but no chemistry-sensitive protocol currently exists for predicting the important experimental value of char yield. The proposed method utilizes a reactive force field (ReaxFF) to model the chemical transformation of precursor monomers into carbonized structures during three processing stages: ramp-up to pyrolysis temperatures (~3000 K), pyrolysis, and quenching. Achieving good agreement with experimental char yields requires continuous removal of small by-product molecules to mimic outgassing, and the application of high pressure to encourage the formation of a dense, glassy network. Six different resin chemistries were investigated: an ethynyl, a phenylethynyl, a cyanate ester, a phthalonitrile, acrylonitrile, and adamantane. These candidates represent a diverse group of precursors with respect to initial cyclic content, presence of heteroatoms, and types of reactive groups. The protocol developed accurately predicts the relative char yield between the investigated chemistries and provides quantitative agreement with experimental values, especially for high char yield resins. Several simulated properties of the carbonized structures are compared with experimental results, including outgassing products, morphology of the final chemical configurations, cyclic content, and mechanical properties.

INTRODUCTION

Carbon matrix composites are light-weight, high-strength materials with great potential for use in extreme temperature applications, such as hypersonic aircraft or spacecraft during atmospheric reentry. Precursor materials are processed for experimental evaluation by subjecting cured samples to temperatures ranging from 600°C to 3000°C *in vacuo*, which causes carbonization and graphitization of the organic polymers. Processing at the higher end of this temperature range results in an essentially pure carbon solid, because all non-carbon elements (heteroatoms) are liberated as small gas molecules. Critically, the thermal and mechanical properties of the resultant carbon materials depend on the final carbon morphology, which is influenced by the precursor chemistry and processing conditions. Important characteristics of the new carbon materials include response to subsequent applications of extreme heat, thermal conductivity, oxidation resistance, and the ability to retain structural integrity or exhibit controlled ablation. Empirical development of high-temperature resins is costly and time consuming. Formulation of the next generation of thermal protection systems will benefit from predictive computational models that accurately simulate experimental conditions.

High char yield is a desirable quality of precursor resin formulations due to the reduced number of subsequent infusion and densification steps necessary to achieve the target density and properties of a material. In order to produce a high char yield, a precursor resin must have the ability to form fused ring structures, rather than degrade into small molecules during late-stage pyrolysis and carbonization. Although there are no clear design rules for formulating precursor resins, common features of frequently used resins include high molecular weight and high degree of aromaticity.[1] Resins that have become widely accepted include furans, phenolics, polyimides, and aryl ethynyls. Typically, the performance of a prospective resin under extreme temperatures is quantified via thermogravimetric analysis (TGA) that involves ramping a sample to carbonization temperatures under an inert atmosphere.[2]

Historically, attempts have been made to correlate resin chemistry with char yield using heuristic formulas fitted with char yield data from the literature. Lyon et al. decomposed the polymer chain into representative moieties, such as phenyl, ester, amide, etc., and weighted each group according to the influence the group had on the polymer's char yield.[3] The authors considered relatively low char yield polymers (less than 50%), and a reasonable correlation for char yield using 38 backbone and side chemical groups was obtained. Parandekar et al. extended this approach by analyzing a similar set of polymers using a quantitative structure-property relationship model that required input of chemical properties such as the HOMO-LUMO gap, aromaticity, and chain branching metrics, rather than weighting specific functional groups.[4] Subsequent analysis confirmed the positive correlation of aromatic and vinyl groups with char yield. Finally, Atabaki et al. designed a simpler approach by identifying correlations that depend only on the number of elements in the polymer repeat unit in conjunction with a limited number of structural units.[5] While these approaches can predict char yield for structurally similar, low char yield polymers, such methods are not readily extended to different chemistries, particularly those known to result in ultrahigh char yields.

Theoretical studies of the carbonization process at the atomistic scale commonly use Monte Carlo methods or reactive molecular dynamics (MD). Reverse Monte Carlo methods have been deployed to generate model carbon fiber morphologies. Such methods first generate an initial large-scale structure that is consistent with a set of experimental observables (e.g., pore size distribution). The starting configuration is then relaxed using a force field,[6,7] such as the reactive empirical bond order (REBO) potential.[8] The introduction and development of more versatile reactive force fields, such as ReaxFF, [9] has facilitated the prediction of glassy carbon morphologies directly through molecular dynamics simulations. [10–13] Two effective ways of generating realistic and independent models are via the 'liquid quench' or 'proxy precursor' method. In the liquid quench method, precursor molecules are converted to a gas of carbon atoms by annealing at extreme temperatures (typically 10,000 K) and quenching back to temperatures of interest to form the solid.[14,15] The proxy precursor method starts with representative aromatic compounds consisting of multiple fused rings, such as naphthalene, larger polycyclic aromatic hydrocarbons, ladder structures, or carbon sheets, and forms a solid by connecting these fragments into larger structures.[16,17] However, neither the liquid quench nor the proxy precursor method are compatible with designing new precursors, because chemical details are lost during the simulation (liquid quench method) or never directly included (proxy precursor method). The weakness of the liquid quench method can be avoided by running longer simulations at annealing temperatures in the vicinity of carbonization temperature. Performing the simulations at a lower temperature avoids complete atomization, which allows for interpretation of the final morphology in terms of the structure of the precursor resin.[18–22] Reactive simulations performed with the lower temperature liquid quench method can predict outgassing products and cure shrinkage during the pyrolysis process, and the post-carbonized system can be characterized by aromatic content, mechanical properties, and pore size distribution. Related studies have adopted these methods to study various properties of carbon fibers, ranging from free surface interactions and kinetics[23,24] to interfacial behavior in carbon-based composites.[25–27]

This modeling effort introduces a protocol optimized to predict the char yield for a given precursor resin chemistry. A ReaxFF parameter set validated for carbonization is used that eliminates the need for detailed prior knowledge of reaction pathways or other empirical formulas for a specific polymer. Practical limitations on simulation size and duration prevent the inclusion of a continuous-flow purge gas (as in TGA) or simulation of the full out-gassing diffusion process, so it was necessary to devise a computationally efficient means of reaching the same end. Simulated outgassing was achieved by employing an open system with a small molecule sink that removes low molecular weight pyrolysis products when produced. The method was validated by simulations on a set of molecules with known charring behavior, including ethynyl and phenylethynyl compounds, a cyanate ester, a phthalonitrile, acrylonitrile, and adamantane. This protocol provides quantitative char yield estimates for precursor resins with a variety of initial aromatic content, heteroatoms, and reactive groups.

METHODS

The dynamics of the pyrolyzing resin precursor were simulated with the reactive force field ReaxFF,[9] as implemented in the LAMMPS molecular dynamics software.[28,29] ReaxFF is a bond order

potential that includes per-element parameters for bonded and nonbonded interactions, angle and torsion contributions, and several correction factors. The force field has recently been parameterized to accurately capture carbon, hydrogen, oxygen and nitrogen interactions, especially during carbonization and graphitization.[20] This updated parameterization is designed to accurately describe small-molecule chemistries that include carbon, hydrogen, oxygen, and nitrogen (CHON-2019), while retaining the accurate parameterizations previously developed for chemistry not including nitrogen (CHO-2016)[30] and graphitic structures.[31] As discussed by Kawalik et al., this parameterization is well-suited to describing carbonization processes that involve small, chemically diverse molecules as precursors, off-gassing products, and the final carbon char configurations of fused carbon rings.[20]

A critical aspect of accurately predicting final char yields and morphologies is the physical treatment of by-products that are released during pyrolysis. The sample is customarily placed in a flowing nitrogen atmosphere during TGA, such that gases that diffuse out of the sample are removed from the surface. In the model developed in this work, there is no free surface from which small molecules can escape, because the simulations use periodic boundary conditions to mimic a bulk material. In addition, the occurrence of such a diffusion process would not be permitted by the accessible simulation time scales. Preliminary simulations were performed using polyarylacetylene resin to evaluate the impact of varying simulation parameters, force fields, and system sizes. These studies included smaller systems (~4000 atoms) modeled with both ReaxFF and the AIREBO force field, and larger systems (~200,000 atoms) modeled with the polymer consistent force field (PCFF), a classical force field, and the REACTER protocol.[32–35] Irrespective of system size or force field, it was discovered that systematic removal of small molecule pyrolysis products was effective in accelerating the pyrolysis process and also improved predictions of product properties, such as density and ring content.

The LAMMPS ReaxFF implementation was modified to allow for deletion of molecules matching a predefined list of compositions or having a mass within a given molecular weight range. Specifically, a feature was added to the '*fix reaxff/species*' command that allows for deletion of molecules matching a user-defined list of structures, using ReaxFF-derived bond orders to determine molecular connectivity. This 'delete' keyword records the time and composition of each molecular deletion for later analysis. The user must specify a frequency for deletion attempts, the bond order cutoff used for determining bond connectivity, and the number of simulation steps that are averaged over in calculating the bond order. This averaging process was necessary because the interatomic distances, upon which the bond order explicitly depends, can deviate beyond typical bonding distances due to thermal fluctuations, particularly at the high temperatures used in these simulations. The spurious deletion of small fragments is avoided, and only stable small molecules are removed, by averaging over several time steps. The incorporation of this feature into the source code, as opposed to using a script-based method, results in a fast implementation for which the efficiency is relatively insensitive to the frequency of deletion attempts or length of the bond order averaging interval. A script-based approach would require stopping and restarting the simulation at each deletion attempt and make the bond order averaging much less efficient. It should be noted that the new implementation results in an open system, rather than a strict ensemble, and is designed to simulate an effectively infinite sink for small gaseous molecules.

Simulation boxes were prepared by adding enough precursor monomers to reach a system size of approximately 32,000 atoms, followed by compression to reach a density of 1.5 g/cm^3, and a 200 ps relaxation run using PCFF. The system was then converted to ReaxFF and equilibrated for another 10 ps to obtain a relaxed initial configuration. A timestep of 0.1 fs was adopted to minimize energy drift for all high-temperature ReaxFF runs, and the Langevin thermostat was employed to achieve simulation stability at extreme temperatures. While larger systems are generally preferred, the need to use the more computationally intensive ReaxFF force field for the simulation of carbonization and subsequent mechanical property determination places practical limits on system size. The system size selected was large enough to allow for full carbonization and retention of enough atoms, after outgassing, to permit statistical analysis and reliable calculation of mechanical properties.

The full protocol used to predict char yield in this work is summarized in Fig. 1, which illustrates the heating, annealing, and cooling stages of char formation. The system is ramped from 300 K to 3000 K at 10 K/ps. This ramp rate is lower than typically used in reactive force field simulations, which allows polymerization reactions, early-stage pyrolysis, and monomer rearrangement to occur during the lower temperature portion of the simulation. The annealing temperature of 3000 K is much higher than

commonly used in TGA experiments, which permits the model to overcome energy barriers that would be insurmountable during accessible simulation time scales. The system was annealed for 270 ps at 3000 K and under 1 GPa of pressure, while periodically removing free small molecules. This annealing duration was sufficient to reach an asymptotic value for char yield. The effect of annealing for longer durations is discussed in the Results section. Approximately 1 GPa was required as the lower limit for simulation pressure to achieve final density values between 1.7 g/cm^3 and 2.0 g/cm^3, similar to that reported for the glassy carbon phase.[36,37] Lower pressures, such as 0.5 GPa, were insufficient to obtain the target densification. During annealing, molecules with a molecular weight less than 50 g/mol were deleted from the system every 0.1 ps. This molecular weight cutoff was selected to remove molecules with three or fewer non-hydrogen atoms. Pairs of atoms with a bond order exceeding 0.3, after averaging over 100 time steps (0.01 ps), were considered bonded for the purpose of identifying molecules for potential deletion. After the annealing stage was complete, the system was cooled to 300 K and equilibrated before further testing and analysis. A strain of 2% and strain rate of 0.1 ns^{-1} were selected for calculating modulus values, to remain in the linear response regime.

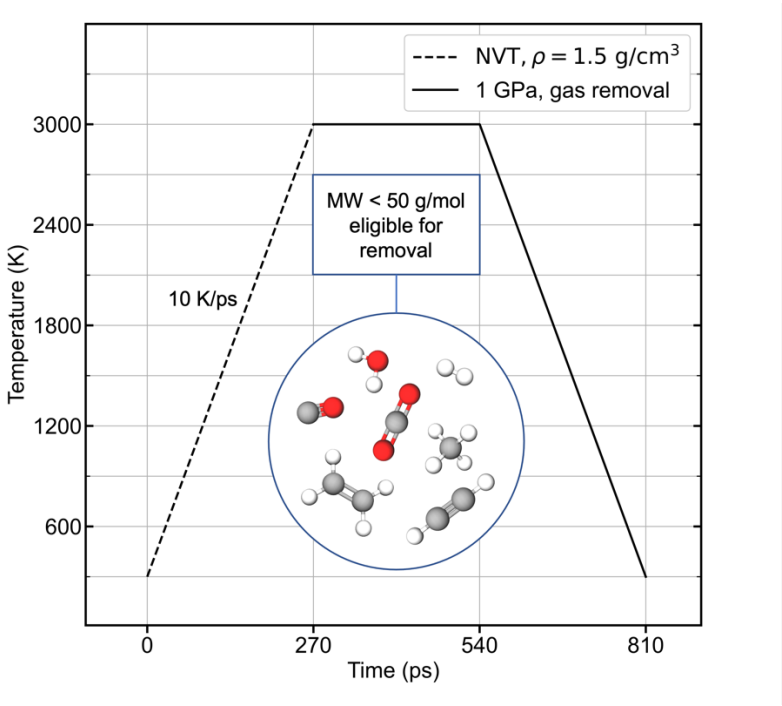

Fig. 1: MD simulation protocol to predict the char yield of a given precursor molecule. By-products with a molecular weight less than 50 g/mol were deleted from the system every 0.1 ps after the system reached the annealing temperature (3000 K).

RESULTS AND DISCUSSION

Results for six resin chemistries with known charring behavior serve to validate the methodology proposed in the Methods section (see Fig. 2). In addition to being well characterized, the structures of these precursor molecules cover a range of aromatic content, functional groups (ethynyl, nitrile, ester, phenol-phthalonitrile), heteroatom content (hydrogen, oxygen, nitrogen) and, most importantly, charring performance. Diethynylbenzene monomers, the precursors for polyarylacetylene (PAA), exhibit exceptionally high char yield, but present processing challenges due to the highly exothermic nature of the decomposing carbon-carbon triple bond. Compared to the precursor molecules for PAA, 1,2,4,5-tetrakis(phenylethynyl)benzene (TPEB) has a lower ratio of ethynyl to aryl groups and reduced

polymerization exothermicity, yet exhibits nearly equivalent char yield performance.[38] Another moiety known to increase char yield is the nitrile group, despite having only one heteroatom (nitrogen) for each carbon atom.[39] Lyon et al. assign the nitrile group a molar contribution equal to its molecular weight, implying that nitrile group content has a strong positive correlation with increasing char yield.[3] Nitrile-containing compounds such as bisphenol A dicyanate ester (BADCY) and phthalonitriles (e.g., the mixture denoted by P1 and defined by Hu et al.[40]) are included in many high-performance polymers and polymer blends.[41,42] Polyacrylonitrile (PAN) has a long history as a low-cost precursor for high-strength carbon fibers and has been well-characterized by the community.[43] Adamantane was chosen as a counterexample that exhibits very low char yield despite being mostly carbon by weight.[44]

The initial carbon content, experimental char yield, and char yield predicted for each structure identified in Fig. 2 are listed in Table 1. The average error for the simulated char yields was ~5 wt.% for these six systems, which is within the range of expected run-to-run variation in experimental results. The char yield results are in good agreement with experimental data, particularly given the extreme conditions that exist during the carbonization process and the use of a heating rate that is much faster than that used in the experiments. Direct comparison of the present method to prior heuristic estimators, such as the molar group method contribution of Lyon et al.,[3] is not productive due to the poor performance of those methods. The molar group contribution method predicts char yields of <40 wt.% for PAA and TPEB, and cannot provide predictions for the behavior of a molecule like adamantane. The poorest predictions of the current method are recorded for molecules containing ether linkages, with an error of ±11 wt.%. Small changes in these more complex chemistries can result in measurable, and in some cases dramatic, differences in char yield. Sakthidharan et al. report a 20 wt.% increase in char yield with the removal of a single carbon atom from the backbone of a cyanate ester compound similar to BADCY.[45] Augustine et al. investigated the temperature resistance of phenol-phthalonitrile chemistries like P1, and reported char yields between 72 wt.% and 78 wt.% (at 900°C), depending on the phthalonitrile content.[46] A second phthalonitrile composition was simulated to assess the ability of the method to reliably predict char yield variation between precursors with subtle structural differences. The second phthalonitrile precursor tested contained ~40% fewer phthalonitrile functional groups than P1, and corresponded to composition P4 in the paper by Hu et al.[40] The predicted and experimental char yields were 69% and 78.5%, respectively, which is the same relative error of ~10% as was found for P1. This result indicated that the simulation method can predict the correct trend in char yield with the same magnitude of error for two precursor compositions with minor differences in chemical structure.

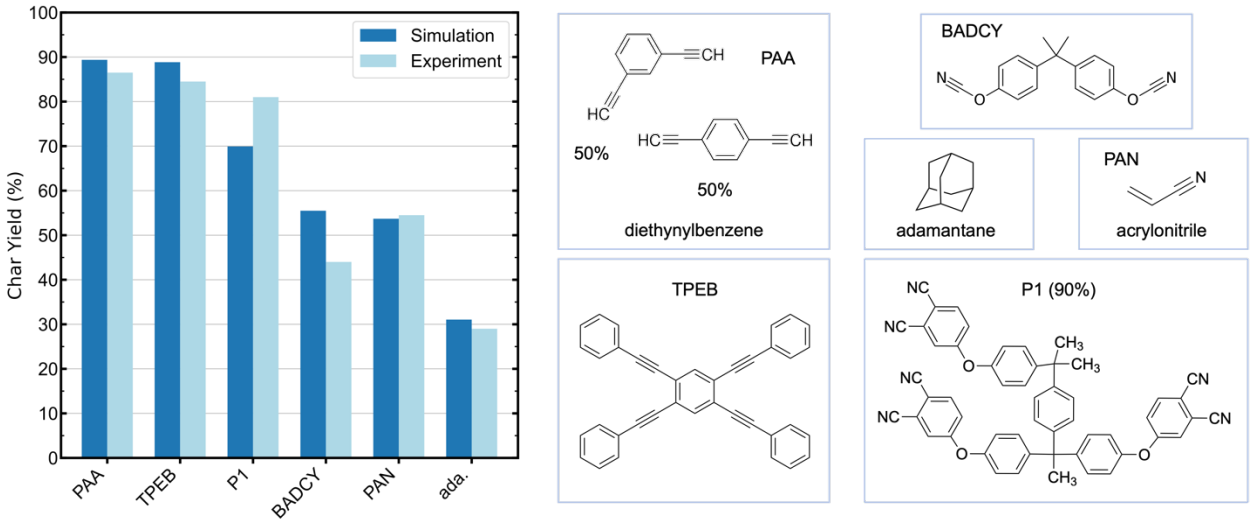

Fig. 2: Predicted and experimental char yields for six resin precursor molecules with the corresponding structures shown on the right. References for experimental values are provided in Table I. PAA and PAN are referred to by polymeric nomenclature, while BADCY, TPEB, etc. are referred to by the precursor molecule. The phthalonitrile compound P1 contains 10% of a di-substituted version of the tri-substituted molecule shown, as described by Hu et al.[40]

Table 1: Total carbon and aromatic carbon content and simulated and experimental char yields for each resin system.

	Initial Carbon Content (wt.%)	Initial Aromatic Carbon (wt.%)	Simulated Char Yield (wt.%)	Experimental Char Yield (wt.%) @ Temp (°C)	Absolute Error in Char Yield (wt.%)
PAA	95	57	89	86 @ 800[47] 87 @ 800[48]	+3
TPEB	95	75	89	85 @ 900[38] 84 @ 1000[49]	+4
P1	79	63	70	81 @ 800[40]	-11
BADCY	73	52	56	45 @ 600[50] 43 @ 800[51]	+11
PAN	68	0	54	55 @ 600[52] 54 @ 800[53]	<1
adamantane	88	0	31	29 @ 675[44]	+2

The computational cost of these simulations is contingent on the ReaxFF force field and the number of atoms, which rendered the approach impractical for exhaustively characterizing the influence of every simulation parameter on the predicted results. However, an effort was made to explore the effect of settings likely to exert the largest impact on the predictions. First, the influence of the initial configuration on the final structure was tested by preparing and carbonizing three independent realizations of the PAA system. The predicted char yields were 89.4%, 89.6%, and 89.7%, which indicates that these systems are large enough that the proper final structure can be reached regardless of the detailed structure of the starting simulation cell. Subsequently, the influence of the length of the annealing phase of the simulation was tested. As shown in Fig. 3, each system experienced a rapid mass loss at the beginning of the annealing phase, when the small molecule removal process was initiated, that reached a plateau by the beginning of the cooling phase, marked by the vertical dashed line at 270 ps. The annealing time was doubled (540 ps) and tripled (810 ps) to ensure further mass loss did not occur at longer times by using the PAA system as a test case. The predicted char yields only slightly declined to 89.2% and 89.1%, respectively, indicating that the charring process was essentially complete at 270 ps. Third, the effect of removing larger by-products was tested by increasing the molecular weight cutoff to 100 g/mol for the PAA system. The predicted char yield decreased by only 0.1% as compared to simulations using the default cutoff of 50 g/mol. Finally, the influence of allowing by-product removal during the heating phase was checked for the BADCY system, which resulted in an increase in final char yield to 57.7%, as compared to 55.5% using the standard protocol. The application of pressure (1 GPa) during the heating phase also resulted in an increase in final char yield to 59.3% for the same system. The increase in char yield in these two test simulations, while small in magnitude, may indicate that the system has reached a marginally more stable configuration after heating than occurs with the standard parameters. In summary, the final predictions that result from the simulations are only weakly dependent on the values chosen, based on the simulation parameters tested.

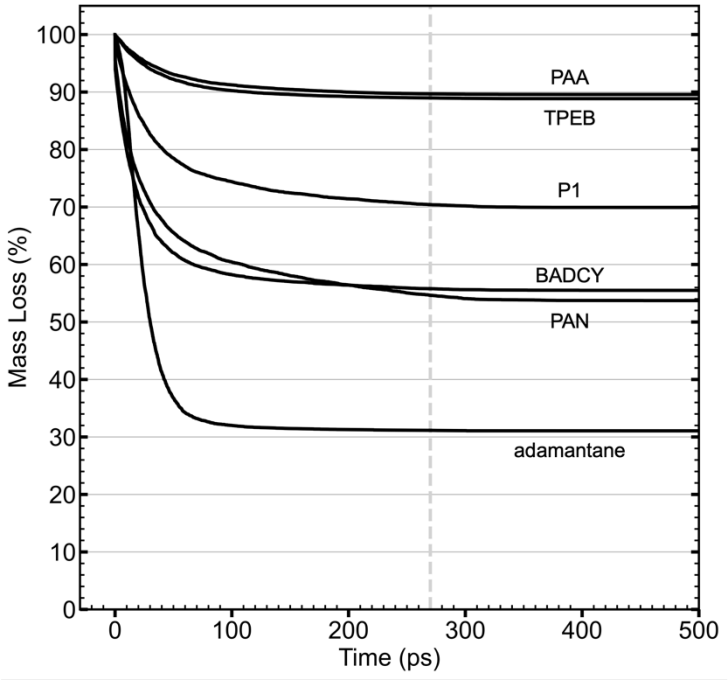

Fig. 3: Mass loss of each system vs. time. In this plot, t = 0 ps corresponds to the start of the annealing stage. The vertical gray dashed line marks the end of the annealing stage and the start of the cooling stage.

The final densities and elastic moduli predicted for each system after equilibration at 300 K are shown in Fig. 4a. The densities fall within ±0.02 g/cm^3 for PAA and BADCY, the two systems for which three independent configurations were simulated. It is notable that the densities do not monotonically increase with increasing char yield, despite the use of identical temperatures and pressures in all simulations (see Fig. 4b). Adamantane, for example, has a similar final density to TPEB, but a much lower char yield. This disparity is a result of adamantane packing more efficiently into the final, smaller simulation cell than does TPEB during the carbonization process. Moduli and other mechanical properties of glassy carbon materials are known to be strongly dependent on density, as reflected in Fig. 4, and the values reported here fall in the range expected from related simulations.[54,55] The mechanical properties predicted in this work are representative of an idealized, defect-free bulk glassy carbon, because porosity (down to the nanoscale) is omitted from the simulated structures. Experimental work has revealed that this effect can be large when porosity was limited by geometrical confinement. The modulus of 4 nm to 6 nm thick glassy carbon thin films (62 GPa) was approximately twice that of bulk glassy carbon (30 GPa).[56]

The stress-strain curves calculated for the PAA and PAN samples, up to 40% uniaxial strain, are shown in Fig. 5. The ultimate tensile strengths of the PAA and PAN systems were ~35 GPa and ~22 GPa, respectively. Similar simulations predicted an ultimate stress of 43 GPa for amorphous carbon at a density of 2.4 g/cm^3, which is quite close to the present value for PAA after dividing by the density of each system to convert to specific strengths.[55] The theoretical value of tensile strength for glassy carbon has been reported as 3 GPa, although no rigorous justification for this value was provided.[57] Experimental comparisons are challenging because the ultimate strength of non-crystalline carbon and other ceramics is highly density and length-scale dependent. For example, the compressive strength of glassy carbon nanopillars has been measured to increase from ~1 GPa to ~7 GPa when the diameter of the pillar is less than 5 μm.[58] The overestimation of ultimate strength reveals a deficiency of atomistic simulations at computationally feasible length scales, and suggests that modifying the model, such as by manual incorporation of larger-scale defects, may be necessary to reproduce the experimentally measured ultimate stress. The extremely high strain rates that must be used in these simulations also contribute to the overestimation of ultimate strength, particularly in systems like these that fail at relatively high strains.

The fact that such large failure strains are reached is, again, a result of the absence of large-scale defects or porosity in the simulated systems. The strength values presented here represent a loose upper bound on the values expected from experiments on real materials due to deficiencies in the models.

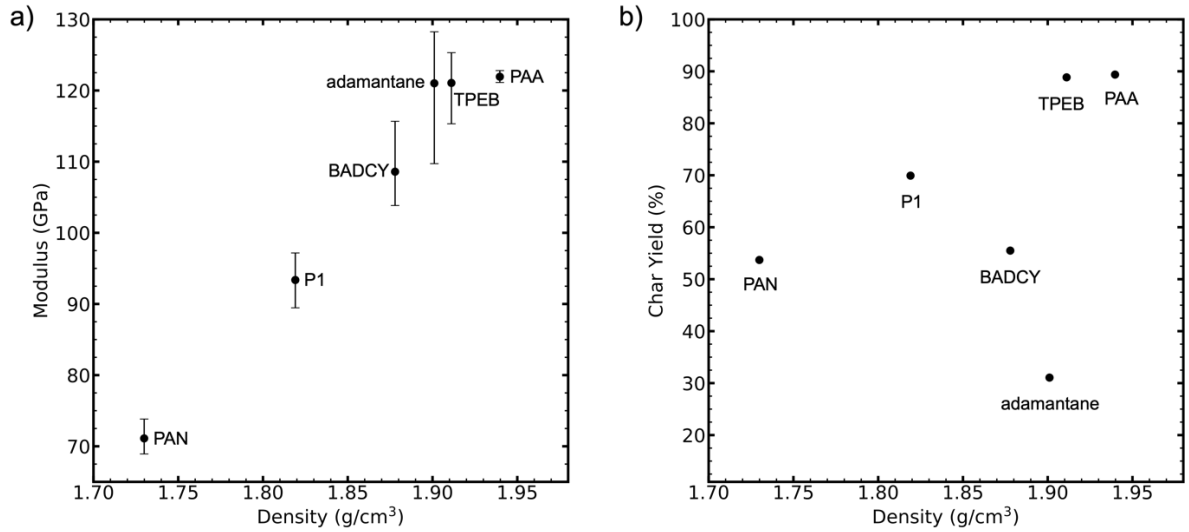

Fig. 4: a) Young's modulus vs. final char density. Moduli are averages over the three axes and the error bars indicate the minimum and maximum values. b) Char yield is not well correlated with final char density.

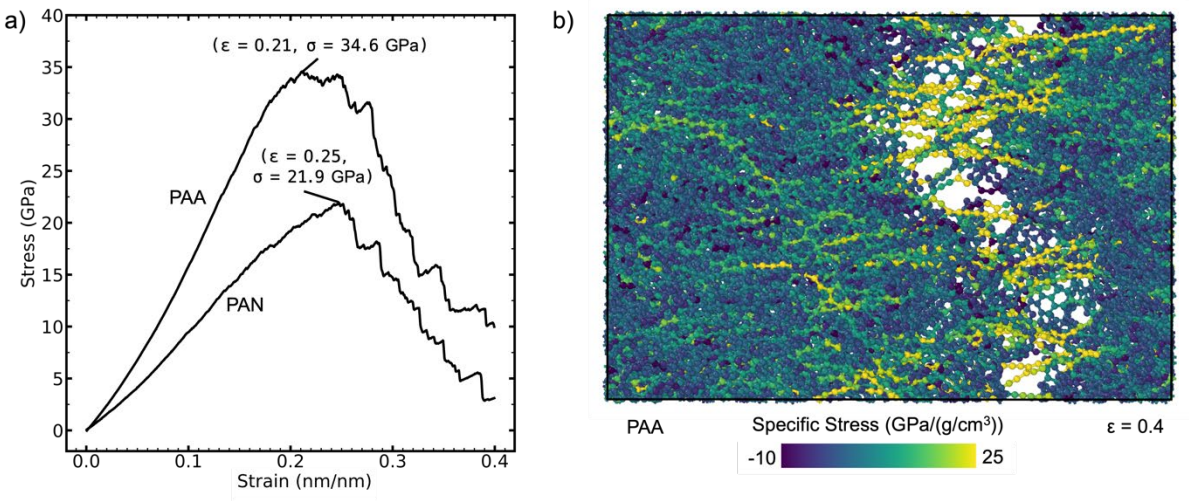

Fig. 5: Carbon chars subjected to uniaxial strain up to 40%. a) Simulated stress-strain curves for PAA and PAN with the point of maximum recorded stress labeled. b) A snapshot of the PAA system colored by instantaneous uniaxial per-atom specific stress at 40% strain, after the formation and propagation of a crack.

The final morphologies for PAA and BADCY are shown in Fig. 6, in which atoms are hidden for clarity and rings are colored by size. The final ring statistics have little dependence on precursor chemistry. Currently, the nanoscale structure of glassy carbon is envisioned as a three-dimensional network of fragments of fullerene-type structures (with positive curvature), segments with negative curvature, and flat nanoribbons. This modern picture is qualitatively consistent with Fig. 6. As shown in Fig. 7a , the final structures were composed of ~25% 5-member, ~50% 6-member and ~25% 7-member

rings, irrespective of the precursor material. Note that larger rings were rarely observed and are not tabulated here. In comparison, C_{60} consists of a 3:5 ratio of 5- and 6-member rings and rings containing more than six atoms are associated with negative curvature.[59] As seen in Fig. 6, the 5- and 7-member rings are uniformly distributed throughout the system. Typically, aromatic nanoribbon segments are rare and are limited to two rings in width and five rings in length. Even though increasing the annealing time did not significantly affect char yield, the ring morphology continued to evolve. An increased incorporation of atoms into rings after doubling and tripling of the annealing time is shown in Fig. 7b. The increase in 5-member rings was negligible, while 480 additional 6-member and 170 additional 7-member rings were formed after tripling the annealing time, which represents a ~12% total increase in ring content.

All samples converged to a composition of primarily sp^2-hybridized carbon during the formation of these fused-ring networks. A ternary phase diagram facilitates visualization of this transformation, where the three 'phases' are defined as sp^2 carbon, non-sp^2 carbon, and heteroatoms (non-carbon), on a per-atom basis.[60] As seen in Fig. 8, the original monomers span a large portion of this phase space, while the chars approach 90% sp^2 carbon, with a large portion of the remaining atoms likely to be under-coordinated carbon at the edge of fused ring clusters.

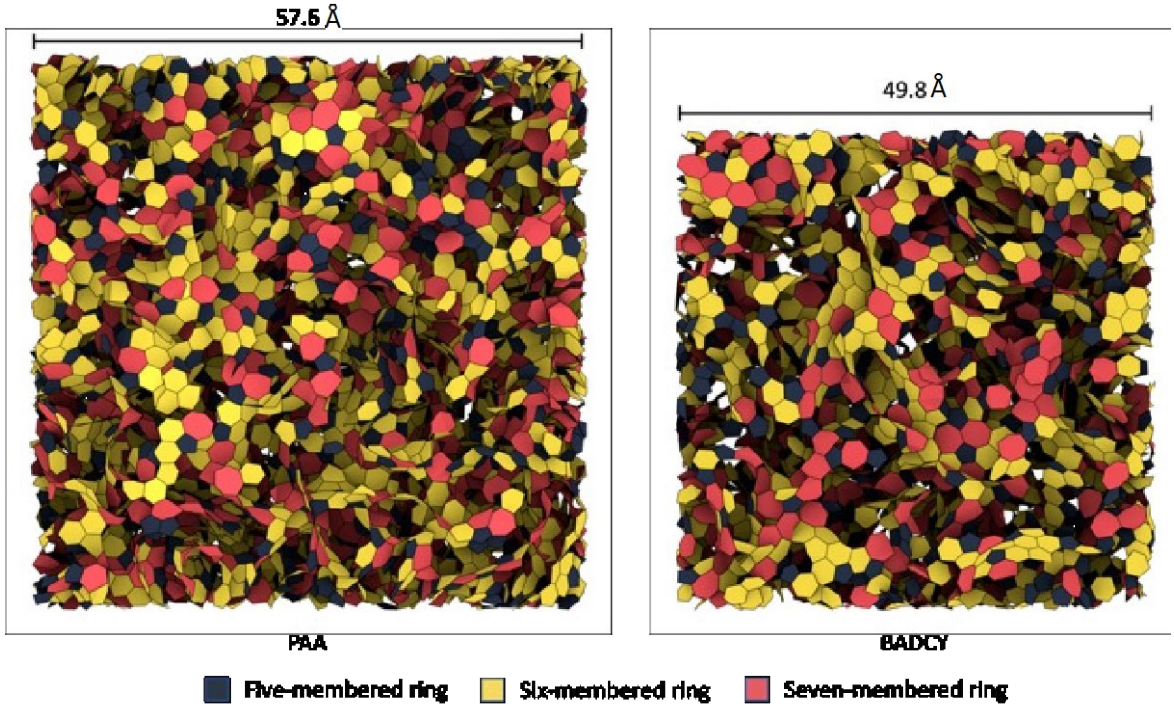

Fig. 6: Final morphologies for a high and moderate char yield system, colored according to ring size. Only 5-, 6- and 7-membered rings not spanning a periodic boundary are shown; other atoms are hidden. The distribution of ring sizes is quantified in Fig. 7.

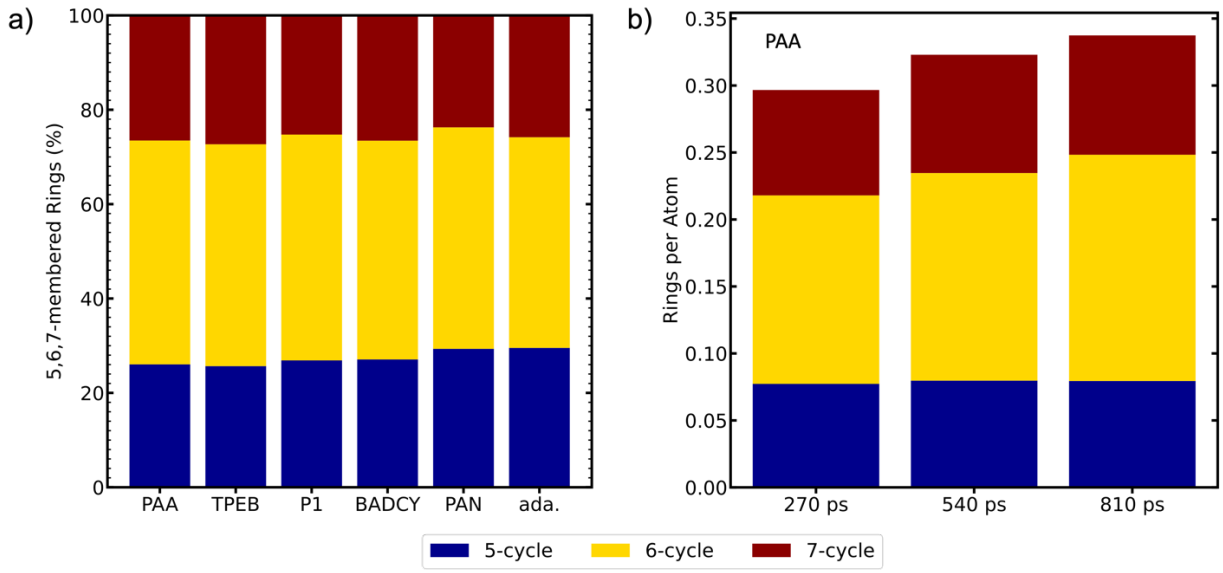

Fig. 7: Ring size statistics for carbonized resins. a) Relative 5-, 6- and 7-membered ring counts reveal similar compositions for all systems. b) Ring counts (divided by number of atoms in the system) vs. annealing time for the PAA sample (this char retained ~19,000 atoms).

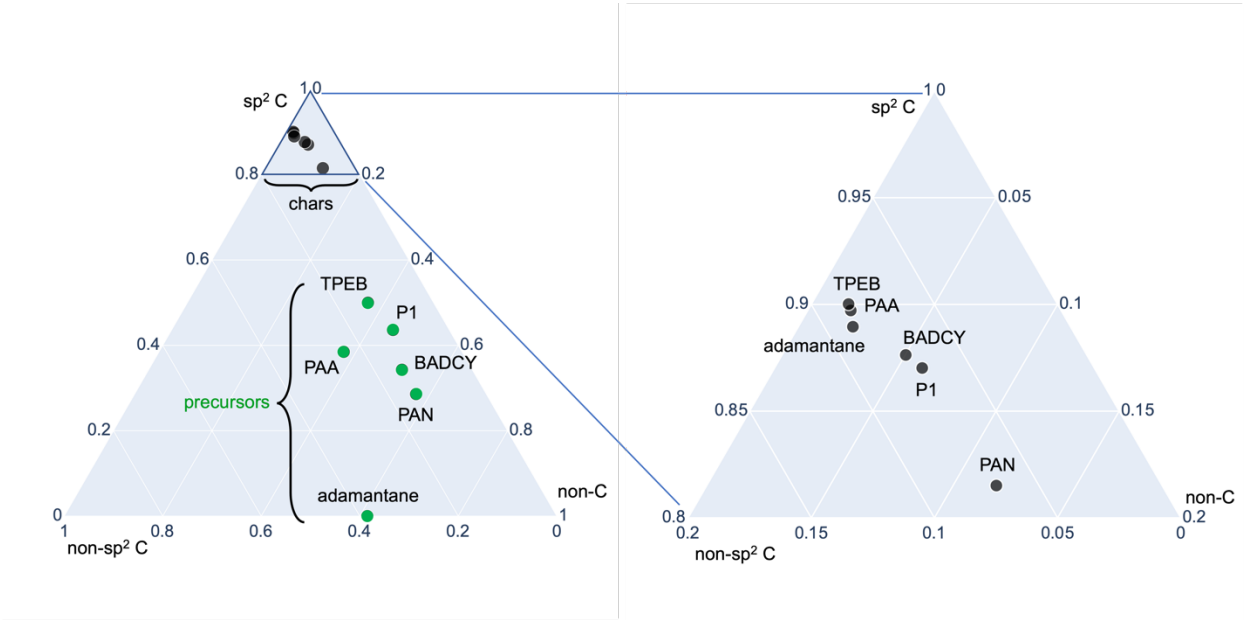

Fig. 8: Ternary phase diagram: Conversion of precursor monomers into fused-ring networks, with respect to carbon hybridization and heteroatom content. The locations of the precursor chemistries are shown in green, and the final carbonized structures are shown in black. Fractions for each atom type are given in terms of atom count.

The atoms remaining after the charring process comprise a single, densely connected network. These glassy carbon networks are complex and difficult to characterize from a topological standpoint. One approach for simplifying this analysis is to convert the atomistic structure into a molecular graph in which the nodes represent individual rings and linkages that are created between the nodes representing pairs of fused rings (see Fig. 9). Clusters are defined as groups of nodes in which each node is linked to at least two other nodes. Additionally, a bridge is defined as a single linkage between two distinct

clusters. A bridge connection is represented on the left side of Fig. 9, where the blue and orange clusters are connected by a single linkage, labeled as a ‘bridge connection’ in the image. In contrast, the image on the right is a single cluster, because every node has at least two links to neighboring nodes. This distinction between linked and contiguous clusters was chosen for this analysis due to the difference in mechanical behavior anticipated for the two structures.

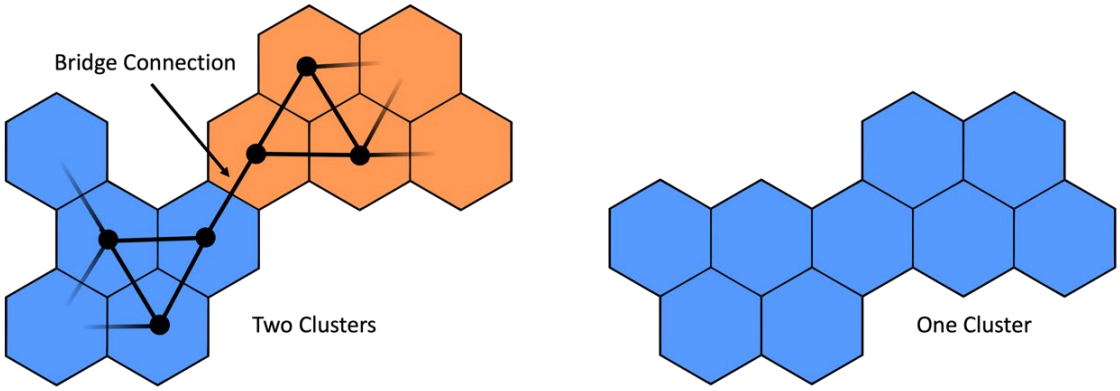

Fig. 9: Clusters within the fused ring network are distinguished using local bridge connections, defined as edges on the reduced (dual) graph such that deleting the edge will locally disconnect two clusters.

The cluster morphologies of the final carbon chars are compared using this analysis method in Fig. 10. PAA and BADCY are visualized in Fig. 10a and Fig. 10b, with the distinct clusters identified by color. Although the difference in the char yields of PAA and BADCY resulted in a large difference in final system size, the clusters are visually similar. Closer inspection of the cluster size distribution reveals some differences that could impact mechanical behavior. Clusters containing up to 10 rings are referred to as small, 10–100 rings as medium, 100–1000 rings as large, and the largest cluster is referred to as the primary cluster. Inspection of Fig. 10c reveals that the primary cluster of the PAA system contains over 50% of the rings in the system. As shown in Fig. 11, this cluster spans the periodic cell in all three directions. The rings that are not a part of the primary cluster are evenly divided between the three smaller categories of cluster size, with each containing 10% to 20% of the total rings. However, the primary cluster for BADCY contains a much smaller fraction of the total number of rings in the system than was the case for PAA. In fact, there are as many total rings involved in small and medium clusters as there are in the primary cluster. As shown in Fig. 10d, this trend continues for lower char yield systems, and may be a symptom of finite box size effects (e.g., the adamantane char contains fewer than 4500 atoms).

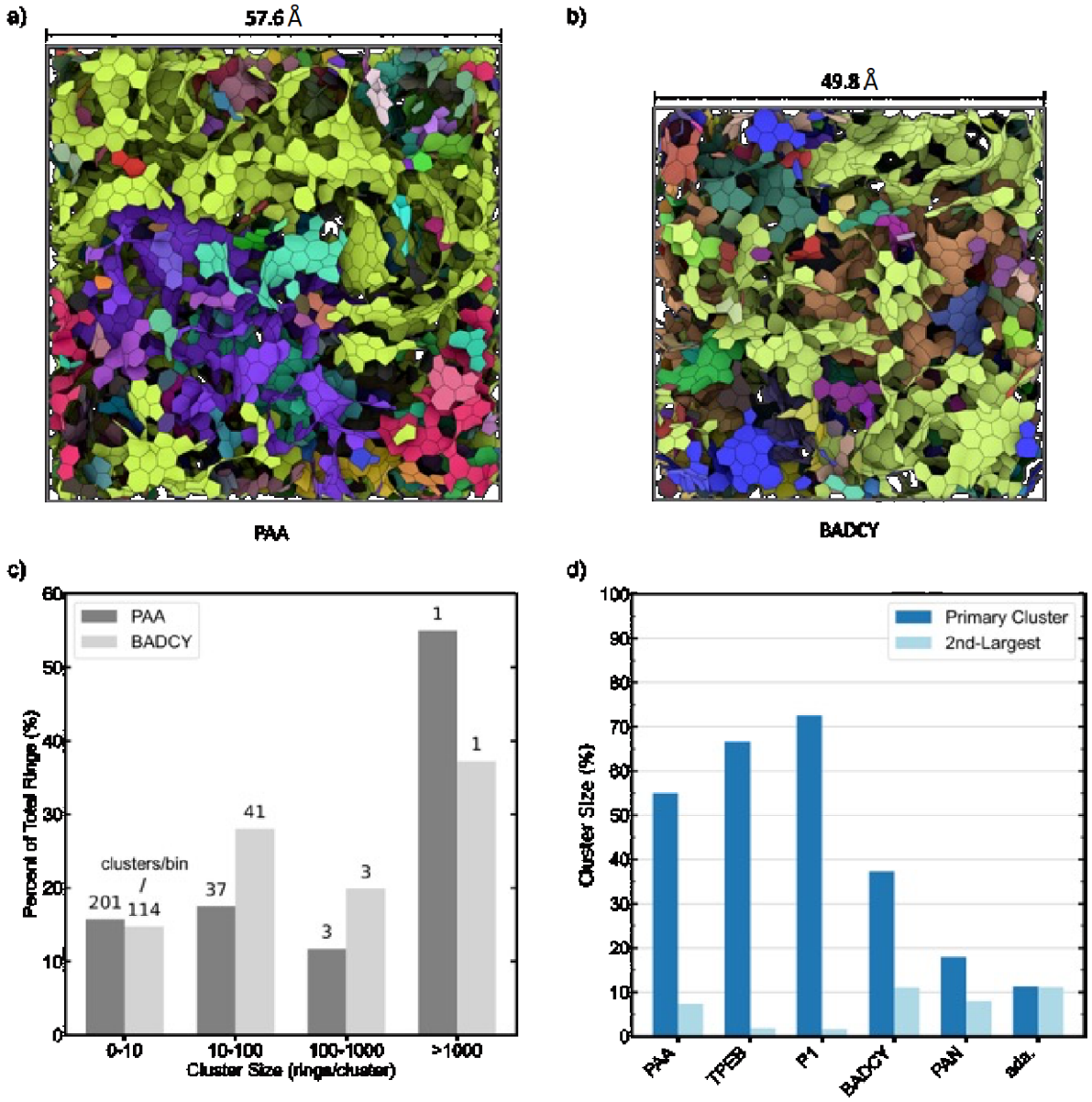

Fig. 10: Cluster analysis of post-carbonization morphologies. a-b) Visualizations of high and moderate char yield systems, with only 5-, 6- and 7-member rings shown and colored according to Fig. 9. c) Cluster size distributions for the systems in frames a and b. d) Relative size of the primary cluster vs. the next largest for all systems. Adamantane is abbreviated as 'ada.' in axis label.

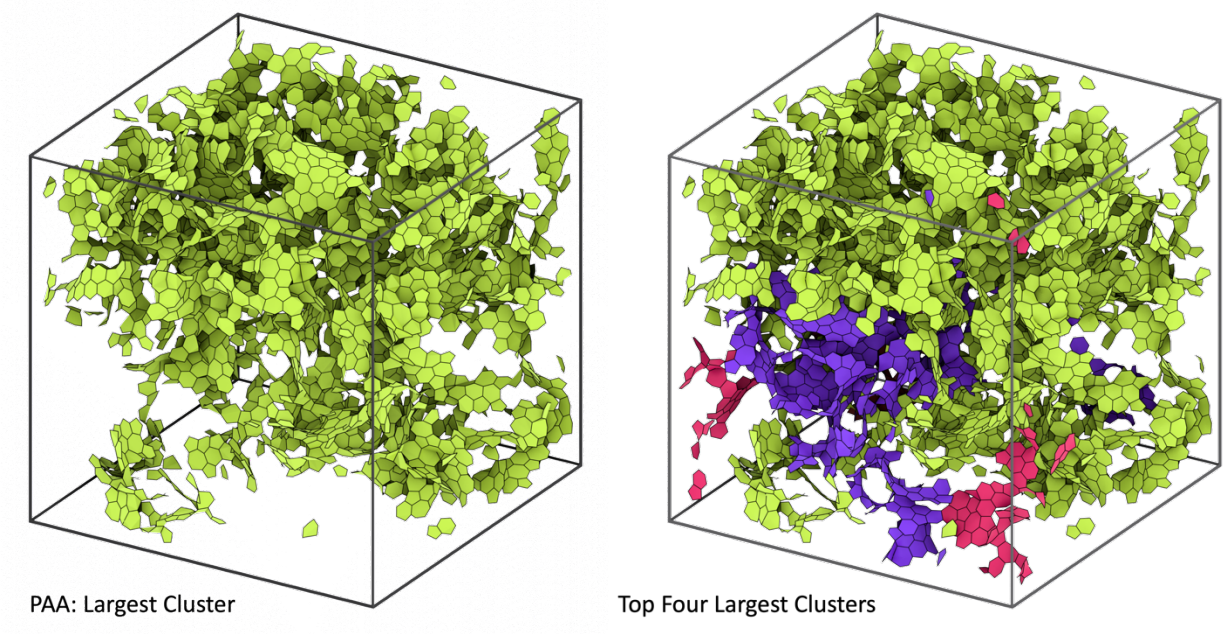

Fig. 11: Visualizing portions of the final PAA carbonized structure. The largest cluster spans the box in all three directions, while the next three largest clusters fill in much of the remaining space (one of these is hidden in this view). Clusters are connected via local bridges.

The composition of the small molecules removed during the pyrolysis simulations were recorded and compared to experimental measurements obtained with infrared spectroscopy and mass spectrometry. The total mass loss from select outgassing products for all systems is shown in Fig. 12. Many different chemical species are produced during the high-temperature reactions; more than 60 unique compounds were removed from the BADCY system at the onset of the annealing stage, mostly in trace amounts. Some of this variety is the result of highly reactive species being removed in the simulation before having time to form more stable products by reacting with other small molecules or free hydrogen atoms in the vicinity. For example, about equal parts CN^- and HCN were removed from the PAN system. It should also be noted that, to simplify the presentation of Fig. 12, some products that were unique to certain precursors (such as ammonia and various nitrogen oxides) are not shown. The types and relative quantities of the species produced generally agree with available data. According to spectroscopic analysis, the primary pyrolysis products of phthalonitrile resins include H_2O, NH_3, HCN, CH_4, CO_2 and CO.[61] These molecules appear in significant amounts in the simulated outgassing products (see Fig. 12), although the relative production of C_2H_2 may be overpredicted. Similar techniques indicate that CO_2 and HNCO are the primary pyrolysis products of BADCY,[62] while the current simulations predict that the off-gas is primarily CO, followed by HNCO and HCN. This disparity may be the result of not allowing sufficient time for secondary reactions prior to removing the small molecules in the simulations.

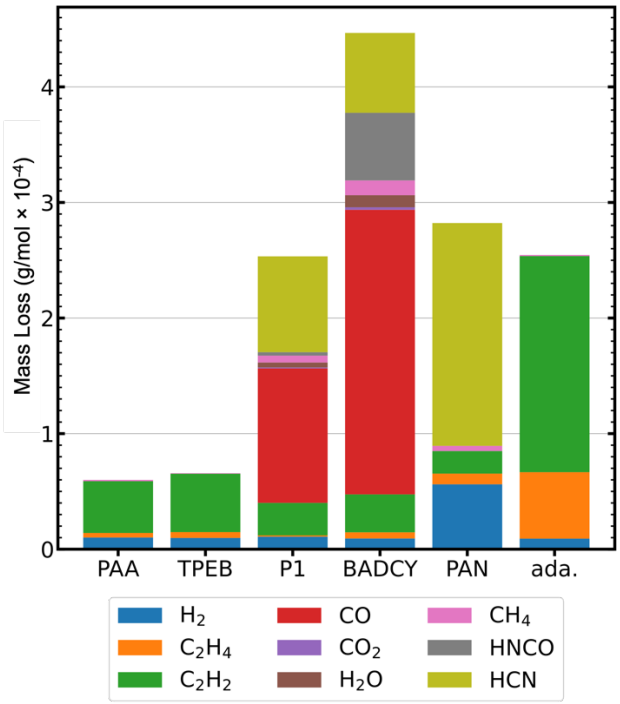

Fig. 12: Total mass of select molecules removed from the simulation during carbonization. To simplify the comparison, a limited number of common pyrolysis products are displayed. For example, the PAN system produced a significant amount of ammonia (not shown).

While it is generally very difficult to characterize the nanoscale structure of amorphous carbon materials, wide-angle X-ray diffraction (WAXD) and high resolution transmission electron microscopy (HRTEM) are two quantitative techniques that can provide some insight.[63,64] The simulated WAXD results are shown in Fig. 13a. The large peak lying between 2θ = 10° and 2θ = 30° in Fig. 13a corresponds to the 002 reflection found in graphitic structures and arises from the interplanar distance between graphitic planes. Compared to crystalline graphite, the peak is broader and shifted to a lower angle, which is commonly seen in amorphous carbon structures. The broadening and shift in position indicate that, while still highly aromatic in character, the amorphous structure lacks the highly ordered structure found in graphitic materials. The smaller 100 reflection seen between 2θ = 40° and 2θ = 45° provides a measure of the lateral crystallite size in polycrystalline carbon systems. This peak is characteristic of glassy carbons generated from organic polymers at lower processing temperatures (<1000ºC),[65] and can also be observed in partially carbonized organic compounds and asphaltenes.[66,67] The 100 peak seen in Fig. 13a is broader and located at a lower angle than is typical for this class of materials, indicating that the crystalline domains in the simulated system are comparatively small. Increasing the annealing time from 270 ps to 810 ps notably sharpened the 002 band in the WAXD spectrum, signifying the development of more compact and better aligned layers of aromatic clusters (see blue curve in Fig. 13a). This trend, coupled with the corresponding increase in six-membered rings shown in Fig. 7b, is indicative of increasing graphitization with extended annealing times.

A simulated HRTEM of the PAA-derived char is shown in Fig. 13b. Jurkiewicz et al. imaged glassy carbon after carbonizing at temperatures ranging from 600ºC to 2500ºC, and the simulated HRTEM image in Fig. 13b bears a closer resemblance to structures carbonized at 600ºC than those heated to 800ºC, above which regions of local graphitization can be observed.[37] Comparison of the simulated WAXD and HRTEM results with comparable experimental results leads to the conclusion that the amorphous structures generated by the present simulations correspond most closely to materials at an early stage of carbonization produced at modest processing temperatures. Longer annealing times, possibly at higher simulated temperatures, would yield structures more similar to the fully carbonized materials produced in the experimental work.

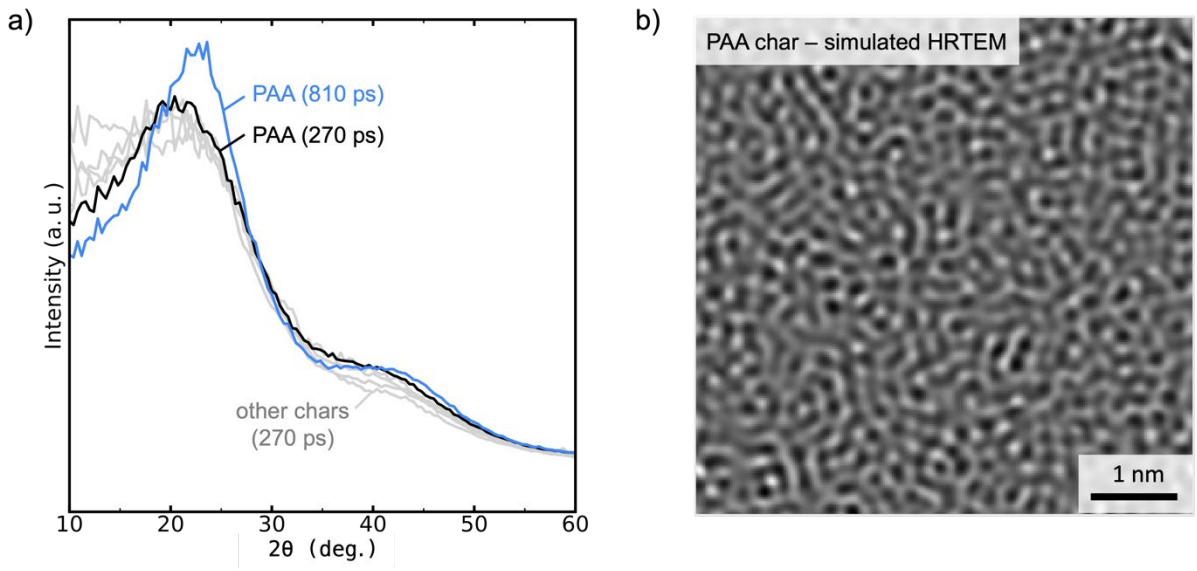

Fig. 13: Simulated versions of common experimental analysis techniques. a) X-ray diffraction patterns for the carbonized systems are typical of amorphous carbon. Increasing the annealing time, given in parentheses, drives the morphology toward a graphitic structure. b) Simulated HRTEM image for the PAA-derived char annealed for 270 ps.

SUMMARY AND CONCLUSIONS

A MD protocol has been developed to predict the char yield of high-temperature resins and provide atomistic models of the resulting char. Analogous to a TGA experiment, the original precursor molecules were subjected to a temperature profile consisting of heating, annealing, and cooling. Employment of a reactive force field (ReaxFF) parameterized for carbon materials facilitated the complex reorganization of atoms and bond topology that occur during pyrolysis. A key feature of the protocol was the systematic removal of small molecules from the system, to mimic the outgassing and subsequent diffusion of by-products into a purge gas. The use of an open system, though unusual in such simulations, was critical to achieving accurate densities and served as an acceleration method to reach beyond the diffusion time scale of small molecules in a glassy carbon matrix. The protocol provided a reproducible and chemistry-specific way to accurately predict the char yield of high-performance resins.

The char yield protocol predicted the high-temperature stability of a diverse set of precursors, including an ethynyl (PAA), a phenylethynyl (TPEB), acrylonitrile (PAN), a phthalonitrile, and a cyanate ester. This set of molecules represented a wide range of initial aromatic and heteroatom content and has char yields ranging from 30 to 90 wt.%. The char yields for each of these precursors have been determined experimentally, and the present protocol was able to reproduce the measured values to an accuracy of 5 wt.% on average. Char yields for the hydrocarbons and acrylonitrile were predicted with ~2 wt.% accuracy on average, while the phenol-phthalonitrile (P1) and cyanate ester (BADCY) simulated yields were within 10 to 12 wt.% of observed values. The result of the carbonization protocol was a dense network of glassy sp^2 carbon consisting of an approximate 2:1:1 ratio of 6-, 5-, and 7-membered rings. The predicted mechanical properties of these densified materials were extremely high and strongly dependent on density, with calculated elastic moduli exceeding 100 GPa for densities above 1.85 g/cm^3. The connectivity of the glassy carbon networks was quantified in terms of fused-ring clusters, but no clear correlation was established with density or elastic moduli. In addition to the char yield, the compositions of simulated by-product gases compared favorably to pyrolysis mass spectrometry results, as did simulated WAXD curves and HRTEM images of the final carbonized material.

The aim of current and future work is to discover novel precursor chemistries that have optimal properties for high-performance resin infusion processes, such as high char yield and low porosity. While this work describes the development and validation of a protocol to model char yield for well-characterized resins, concurrent efforts (both modeling and experimental) are underway to explore new chemistries with previously unknown char behavior. The results presented here confirm the predictive power and chemistry-sensitive capability of the protocol, particularly for ultrahigh char yield resins. In conclusion, the protocol is a promising tool for efficiently screening ideas for next-generation resins in conjunction with experimental efforts.

ACKNOWLEDGMENTS

J.R.G. appreciates technical guidance from Benjamin Jensen. Resources supporting this work were provided by the NASA High-End Computing (HEC) Program through the NASA Advanced Supercomputing (NAS) Division at Ames Research Center.

REFERENCES

1. Savage, G. *Carbon-Carbon Composites*; Springer Netherlands: Dordrecht, 1993.
2. Wilkie, C. A. TGA/FTIR: An Extremely Useful Technique for Studying Polymer Degradation. *Polymer Degradation and Stability* **1999**, *66* (3), 301–306.
3. Lyon, R. E.; Takemori, M. T.; Safronava, N.; Stoliarov, S. I.; Walters, R. N. A Molecular Basis for Polymer Flammability. *Polymer* **2009**, *50* (12), 2608–2617.
4. Parandekar, P. V.; Browning, A. R.; Prakash, O. Modeling the Flammability Characteristics of Polymers Using Quantitative Structure–Property Relationships (QSPR). *Polymer Engineering & Science* **2015**, *55* (7), 1553–1559.
5. Atabaki, F.; Keshavarz, M. H.; Noorollahy Bastam, N. A Simple Method for the Reliable Prediction of Char Yield of Polymers. *Zeitschrift für anorganische und allgemeine Chemie* **2017**, *643* (16), 1049–1056.
6. Nguyen, T. X.; Cohaut, N.; Bae, J.-S.; Bhatia, S. K. New Method for Atomistic Modeling of the Microstructure of Activated Carbons Using Hybrid Reverse Monte Carlo Simulation. *Langmuir* **2008**, *24* (15), 7912–7922.
7. Farbos, B.; Weisbecker, P.; Fischer, H. E.; Da Costa, J.-P.; Lalanne, M.; Chollon, G.; Germain, C.; Vignoles, G. L.; Leyssale, J.-M. Nanoscale Structure and Texture of Highly Anisotropic Pyrocarbons Revisited with Transmission Electron Microscopy, Image Processing, Neutron Diffraction and Atomistic Modeling. *Carbon* **2014**, *80*, 472–489.
8. Brenner, D. W.; Shenderova, O. A.; Harrison, J. A.; Stuart, S. J.; Ni, B.; Sinnott, S. B. A Second-Generation Reactive Empirical Bond Order (REBO) Potential Energy Expression for Hydrocarbons. *J. Phys.: Condens. Matter* **2002**, *14* (4), 783–802.
9. van Duin, A. C. T.; Dasgupta, S.; Lorant, F.; Goddard, W. A. ReaxFF: A Reactive Force Field for Hydrocarbons. *J. Phys. Chem. A* **2001**, *105* (41), 9396–9409.
10. de Tomas, C.; Suarez-Martinez, I.; Marks, N. A. Graphitization of Amorphous Carbons: A Comparative Study of Interatomic Potentials. *Carbon* **2016**, *109*, 681–693.
11. Li, K.; Zhang, H.; Li, G.; Zhang, J.; Bouhadja, M.; Liu, Z.; Skelton, A. A.; Barati, M. ReaxFF Molecular Dynamics Simulation for the Graphitization of Amorphous Carbon: A Parametric Study. *J. Chem. Theory Comput.* **2018**, *14* (5), 2322–2331.
12. Orekhov, N.; Ostroumova, G.; Stegailov, V. High Temperature Pure Carbon Nanoparticle Formation: Validation of AIREBO and ReaxFF Reactive Molecular Dynamics. *Carbon* **2020**, *170*, 606–620.

13. Montgomery-Walsh, R.; Nimbalkar, S.; Bunnell, J.; Galindo, S. L.; Kassegne, S. Molecular Dynamics Simulation of Evolution of Nanostructures and Functional Groups in Glassy Carbon under Pyrolysis. *Carbon* **2021**, *184*, 627–640.
14. Ranganathan, R.; Rokkam, S.; Desai, T.; Keblinski, P. Generation of Amorphous Carbon Models Using Liquid Quench Method: A Reactive Molecular Dynamics Study. *Carbon* **2017**, *113*, 87–99.
15. Vuković, F.; Walsh, T. R. Practical Atomistic Models of Carbon Fiber Surfaces with Tuneable Topology and Topography. *Composites Science and Technology* **2021**, *216*, 109049.
16. Joshi, K.; Arefev, M. I.; Zhigilei, L. V. Generation and Characterization of Carbon Fiber Microstructures by Atomistic Simulations. *Carbon* **2019**, *152*, 396–408.
17. Jian, C.; Merchant, S.; Zang, X.; Ferralis, N.; Grossman, J. C. Structural Evolutions of Small Aromatic Mixtures under Extreme Temperature Conditions: Insights from ReaxFF Molecular Dynamics Investigations. *Carbon* **2019**, *155*, 309–319.
18. Jiang, D.; van Duin, A. C. T.; Goddard, W. A.; Dai, S. Simulating the Initial Stage of Phenolic Resin Carbonization via the ReaxFF Reactive Force Field. *J. Phys. Chem. A* **2009**, *113* (25), 6891–6894.
19. Saha, B.; Schatz, G. C. Carbonization in Polyacrylonitrile (PAN) Based Carbon Fibers Studied by ReaxFF Molecular Dynamics Simulations. *J. Phys. Chem. B* **2012**, *116* (15), 4684–4692.
20. Kowalik, M.; Ashraf, C.; Damirchi, B.; Akbarian, D.; Rajabpour, S.; van Duin, A. C. T. Atomistic Scale Analysis of the Carbonization Process for C/H/O/N-Based Polymers with the ReaxFF Reactive Force Field. *J. Phys. Chem. B* **2019**, *123* (25), 5357–5367.
21. Mao, Q.; Rajabpour, S.; Kowalik, M.; van Duin, A. C. T. Predicting Cost-Effective Carbon Fiber Precursors: Unraveling the Functionalities of Oxygen and Nitrogen-Containing Groups during Carbonization from ReaxFF Simulations. *Carbon* **2020**, *159*, 25–36.
22. Jian, C.; Adams, J. J.; Grossman, J. C.; Ferralis, N. Carbon Fiber Synthesis from Pitch: Insights from ReaxFF Based Molecular Dynamics Simulations. *Carbon* **2021**, *176*, 569–579.
23. Chen, M.; Zhu, Y.; Xia, J.; Wu, H. Molecular Insights into the Initial Formation of Pyrolytic Carbon upon Carbon Fiber Surface. *Carbon* **2019**, *148*, 307–316.
24. Shi, L.; Sessim, M.; Tonks, M. R.; Phillpot, S. R. Generation and Characterization of an Improved Carbon Fiber Model by Molecular Dynamics. *Carbon* **2021**, *173*, 232–244.
25. Saha, B.; Furmanchuk, A.; Dzenis, Y.; Schatz, G. C. Multi-Step Mechanism of Carbonization in Templated Polyacrylonitrile Derived Fibers: ReaxFF Model Uncovers Origins of Graphite Alignment. *Carbon* **2015**, *94*, 694–704.
26. Jensen, B. D.; Odegard, G. M.; Kim, J.-W.; Sauti, G.; Siochi, E. J.; Wise, K. E. Simulating the Effects of Carbon Nanotube Continuity and Interfacial Bonding on Composite Strength and Stiffness. *Composites Science and Technology* **2018**, *166*, 10–19.
27. Rajabpour, S.; Mao, Q.; Gao, Z.; Khajeh Talkhoncheh, M.; Zhu, J.; Schwab, Y.; Kowalik, M.; Li, X.; van Duin, A. C. T. Low-Temperature Carbonization of Polyacrylonitrile/Graphene Carbon Fibers: A Combined ReaxFF Molecular Dynamics and Experimental Study. *Carbon* **2021**, *174*, 345–356.
28. Aktulga, H. M.; Fogarty, J. C.; Pandit, S. A.; Grama, A. Y. Parallel Reactive Molecular Dynamics: Numerical Methods and Algorithmic Techniques. *Parallel Computing* **2012**, *38* (4), 245–259.
29. Thompson, A. P.; Aktulga, H. M.; Berger, R.; Bolintineanu, D. S.; Brown, W. M.; Crozier, P. S.; in 't Veld, P. J.; Kohlmeyer, A.; Moore, S. G.; Nguyen, T. D.; Shan, R.; Stevens, M. J.; Tranchida, J.; Trott, C.; Plimpton, S. J. LAMMPS - a Flexible Simulation Tool for Particle-Based Materials Modeling at the Atomic, Meso, and Continuum Scales. *Computer Physics Communications* **2022**, *271*, 108171.
30. Ashraf, C.; van Duin, A. C. T. Extension of the ReaxFF Combustion Force Field toward Syngas Combustion and Initial Oxidation Kinetics. *J. Phys. Chem. A* **2017**, *121* (5), 1051–1068.
31. Srinivasan, S. G.; van Duin, A. C. T.; Ganesh, P. Development of a ReaxFF Potential for Carbon Condensed Phases and Its Application to the Thermal Fragmentation of a Large Fullerene. *J. Phys. Chem. A* **2015**, *119* (4), 571–580.
32. O'Connor, T. C.; Andzelm, J.; Robbins, M. O. AIREBO-M: A Reactive Model for Hydrocarbons at Extreme Pressures. *J. Chem. Phys.* **2015**, *142* (2), 024903.
33. Sun, H.; Mumby, S. J.; Maple, J. R.; Hagler, A. T. An Ab Initio CFF93 All-Atom Force Field for Polycarbonates. *Journal of the American Chemical Society* **1994**, *116* (7), 2978–2987.

34. Gissinger, J. R.; Jensen, B. D.; Wise, K. E. REACTER: A Heuristic Method for Reactive Molecular Dynamics. *Macromolecules* **2020**, *53* (22), 9953–9961.
35. Gissinger, J. R.; Jensen, B. D.; Wise, K. E. Modeling Chemical Reactions in Classical Molecular Dynamics Simulations. *Polymer* **2017**, *128*, 211–217.
36. Stephens, E. B.; Tour, J. M. Metal-Catalyzed Alkynylation of Brominated Polyphenylenes. Thermoset Precursors of High-Density Monolithic Glassy Carbon. *Macromolecules* **1993**, *26* (10), 2420–2427.
37. Jurkiewicz, K.; Pawlyta, M.; Zygadło, D.; Chrobak, D.; Duber, S.; Wrzalik, R.; Ratuszna, A.; Burian, A. Evolution of Glassy Carbon under Heat Treatment: Correlation Structure–Mechanical Properties. *J Mater Sci* **2018**, *53* (5), 3509–3523.
38. Keller, T. M.; Jones, K. M. Aromatic Acetylenes as Carbon Precursors. US5980853A, November 9, 1999.
39. Gissinger, J. R.; Pramanik, C.; Newcomb, B.; Kumar, S.; Heinz, H. Nanoscale Structure–Property Relationships of Polyacrylonitrile/CNT Composites as a Function of Polymer Crystallinity and CNT Diameter. *ACS Appl. Mater. Interfaces* **2017**.
40. Hu, Y.; Weng, Z.; Qi, Y.; Wang, J.; Zhang, S.; Liu, C.; Zong, L.; Jian, X. Self-Curing Triphenol A-Based Phthalonitrile Resin Precursor Acts as a Flexibilizer and Curing Agent for Phthalonitrile Resin. *RSC Advances* **2018**, *8* (57), 32899–32908.
41. Hamerton, I. *Chemistry and Technology of Cyanate Ester Resins*; Springer Science & Business Media, 2012.
42. Derradji, M.; Jun, W.; Wenbin, L. *Phthalonitrile Resins and Composites: Properties and Applications*; William Andrew, 2018.
43. Nataraj, S. K.; Yang, K. S.; Aminabhavi, T. M. Polyacrylonitrile-Based Nanofibers—A State-of-the-Art Review. *Progress in Polymer Science* **2012**, *37* (3), 487–513.
44. Kazanskii, B. A.; Shokova, É. A.; Korosteleva, T. V. The Pyrolysis of Adamantane. *Russ Chem Bull* **1968**, *17* (11), 2506–2508.
45. Sakthidharan, C. P.; Sundararajan, P. R.; Sarojadevi, M. Thermal and Mechanical Properties of Azomethine Functionalized Cyanate Ester/Epoxy Blends. *RSC Adv.* **2015**, *5* (25), 19666–19674.
46. Augustine, D.; Mathew, D.; Nair, C. P. R. Phenol-Containing Phthalonitrile Polymers – Synthesis, Cure Characteristics and Laminate Properties. *Polymer International* **2013**, *62* (7), 1068–1076.
47. Tseng, W.-C.; Chen, Y.; Chang, G.-W. Curing Conditions of Polyarylacetylene Prepolymers to Obtain Thermally Resistant Materials. *Polymer Degradation and Stability* **2009**, *94* (12), 2149–2156.
48. Qi, H.; Pan, G.; Yin, L.; Zhuang, Y.; Huang, F.; Du, L. Preparation and Characterization of High Char Yield Polybenzoxazine/Polyarylacetylene Blends for Resin-Transfer Molding. *Journal of Applied Polymer Science* **2009**, *114* (5), 3026–3033.
49. Butler, T.; Alden, S. E.; Taylor, M.; Deese, S.; Rider, D. A.; Laskoski, M. Oligomeric Phthalonitriles and Tetrakis(Phenylethynyl)Benzene Blends with Improved Processing and Thermal Properties. *Journal of Polymer Science Part A: Polymer Chemistry* **2018**, *56* (23), 2630–2640.
50. Wang, Y.; Kou, K.; Zhao, W.; Wu, G.; Han, F. The Effect of Functionalized Benzoxazine with Allyl Groups on the Dielectric, Mechanical and Thermal Properties of BMI/BADCy Composites. *RSC Adv.* **2015**, *5* (120), 99313–99321.
51. Dai, S.; Zhuo, D.; Gu, A.; Liang, G.; Yuan, L. A Novel Hybrid Catalyst System and Its Effects on the Curing, Thermal, and Dielectric Properties of Cyanate Ester. *Polymer Engineering & Science* **2011**, *51* (11), 2236–2244.
52. Song, C.; Wang, T.; Qiu, Y.; Qiu, J.; Cheng, H. Effect of Carbonization Atmosphere on the Structure Changes of PAN Carbon Membranes. *J Porous Mater* **2009**, *16* (2), 197–203.
53. Tay, Y. S.; Liu, M.; Lim, J. S. K.; Chen, H.; Hu, X. Phthalonitrile Prepolymer and PAN Blends: New Strategy for Precursor Stabilization and Pyrolytic Char Yield Enhancement. *Polymer Degradation and Stability* **2020**, *172*, 109056.
54. Wang, Y.; Fan, Z.; Qian, P.; Ala-Nissila, T.; Caro, M. A. Structure and Pore Size Distribution in Nanoporous Carbon. *Chem. Mater.* **2022**, *34* (2), 617–628.
55. Jensen, B. D.; Wise, K. E.; Odegard, G. M. Simulation of the Elastic and Ultimate Tensile Properties of Diamond, Graphene, Carbon Nanotubes, and Amorphous Carbon Using a Revised ReaxFF Parametrization. *J. Phys. Chem. A* **2015**, *119* (37), 9710–9721.

56. Manoharan, M.; Lee, H.; Rajagopalan, R.; Foley, H.; Haque, M. Elastic Properties of 4–6 Nm-Thick Glassy Carbon Thin Films. *Nanoscale Res Lett* **2009**, *5* (1), 14–19.
57. Bauer, J.; Schroer, A.; Schwaiger, R.; Kraft, O. Approaching Theoretical Strength in Glassy Carbon Nanolattices. *Nature Mater* **2016**, *15* (4), 438–443.
58. Albiez, A.; Schwaiger, R. Size Effect on the Strength and Deformation Behavior of Glassy Carbon Nanopillars. *MRS Advances* **2019**, *4* (2), 133–138.
59. Martin, J. W.; de Tomas, C.; Suarez-Martinez, I.; Kraft, M.; Marks, N. A. Topology of Disordered 3D Graphene Networks. *Phys. Rev. Lett.* **2019**, *123* (11), 116105.
60. Zhang, L.; Wei, X.; Lin, Y.; Wang, F. A Ternary Phase Diagram for Amorphous Carbon. *Carbon* **2015**, *94*, 202–213.
61. Liang, B.; Wang, J.; Hu, J.; Li, C.; Li, R.; Liu, Y.; Zeng, K.; Yang, G. TG-MS-FTIR Study on Pyrolysis Behavior of Phthalonitrile Resin. *Polymer Degradation and Stability* **2019**, *169*, 108954.
62. Ramirez, M. L.; Walters, R.; Lyon, R. E.; Savitski, E. P. Thermal Decomposition of Cyanate Ester Resins. *Polymer Degradation and Stability* **2002**, *78* (1), 73–82.
63. Coleman, S. P.; Spearot, D. E.; Capolungo, L. Virtual Diffraction Analysis of Ni [0 1 0] Symmetric Tilt Grain Boundaries. *Modelling Simul. Mater. Sci. Eng.* **2013**, *21* (5), 055020.
64. Rangel DaCosta, L.; Brown, H. G.; Pelz, P. M.; Rakowski, A.; Barber, N.; O'Donovan, P.; McBean, P.; Jones, L.; Ciston, J.; Scott, M. C.; Ophus, C. Prismatic 2.0 – Simulation Software for Scanning and High Resolution Transmission Electron Microscopy (STEM and HRTEM). *Micron* **2021**, *151*, 103141.
65. Bukalov, S. S.; Zubavichus, Y. V.; Leites, L.; Sorokin, A. I.; Kotosonov, A. S. Structural Changes in Industrial Glassy Carbon as a Function of Heat Treatment Temperature According to Raman Spectroscopy and X-Ray Diffraction Data. *Nanosyst. Phys. Chem. Math.* **2014**, *5*, 186–191.
66. Sadeghtabaghi, Z.; Rabbani, A. R.; Hemmati-Sarapardeh, A. A Review on Asphaltenes Characterization by X-Ray Diffraction: Fundamentals, Challenges, and Tips. *Journal of Molecular Structure* **2021**, *1238*, 130425.
67. Suganuma, S.; Nakajima, K.; Kitano, M.; Yamaguchi, D.; Kato, H.; Hayashi, S.; Hara, M. Hydrolysis of Cellulose by Amorphous Carbon Bearing SO3H, COOH, and OH Groups. *J. Am. Chem. Soc.* **2008**, *130* (38), 12787–12793.